
Shape and Topology Optimization for Periodic Problems

Part II: Optimization algorithm and numerical examples

Cristian Barbarosie · Anca-Maria Toader

Preprint CMAF Pre-2008-017 <http://cmaf.ptmat.fc.ul.pt/preprints/preprints.html>

Abstract The present paper deals with the implementation of an optimization algorithm for periodic problems which alternates shape and topology optimization (the theoretical background about shape and topological derivatives was developed in Part I [7]). The proposed numerical code lays on a special implementation of the periodicity conditions based on differential geometry concepts: periodic functions are viewed as functions defined on a torus. Moreover the notion of periodicity is extended and cases where the periodicity cell is a general parallelogram are admissible. This approach can be adapted to other frameworks (fluids, cable design, etc.). The numerical method was tested for the design of periodic microstructures. Several examples of optimal microstructures are given for bulk modulus maximization, maximization of rigidity for shear response, maximization of rigidity in a prescribed direction, minimization of the Poisson coefficient.

Keywords Optimization of Microstructures · Finite Element Method on a Periodic Mesh · Mesh Regeneration · Shape Optimization · Topology Optimization · Auxetic Materials

1 Introduction

The main motivation of the present paper comes from the study of periodic microstructures and optimization of their

macroscopic properties, in the context of linearized elasticity. A periodic microstructure is a body whose material coefficients vary at a microscopic scale, according to a periodic pattern. Homogenization theory allows one to accurately describe the macroscopic behaviour of such a microstructure by means of so-called cellular problems, which are elliptic PDEs subject to periodicity conditions. Porous materials, that is, bodies with periodic infinitesimal perforations, can be described in a similar manner.

This is the second of a series of two papers; it contains the numerical implementation and results of an optimization method for periodic microstructures, based on the shape and topological derivatives in the periodic framework (see Part I [7]). However the present paper is self-contained in the sense that for the reader who is not interested in the calculations of the shape and topological derivatives, their formulae are stated without proofs. The main ingredient of the present paper is a numerical code for periodic problems. Some preliminary results were presented in [14]. The treatment given to the periodicity conditions is quite flexible and easy to adapt to other frameworks, for example to fluid dynamics problems subject to periodicity conditions (see e. g. [15]).

Section 2 presents the cellular problem that governs the behaviour of a porous media with periodic microstructure. The properties of the effective material are optimized by minimizing a cost functional (6) under a volume constraint. The numerical algorithm in Section 3 is based on an alternate scheme between shape and topology optimization. Once the cellular problem is solved, both shape and topology derivatives may be used to determine alternatively steepest descent directions. Following these directions, the cellular geometry varies, either by variation of the shape of the hole, by introduction of holes or by merging of existing holes. The finite element method employed to solve the cellular problem is adapted to periodic problems (see Section 4). The mesh used for the cellular domain is seen like

C. Barbarosie
CMAF Av. Prof. Gama Pinto, 2, 1649-003, Lisbon, Portugal
Tel.: +351-217904919
Fax: +351-217954288
E-mail: barbaros@ptmat.fc.ul.pt

A.-M. Toader
CMAF Av. Prof. Gama Pinto, 2, 1649-003, Lisbon, Portugal
Tel.: +351-217904918
Fax: +351-217954288

laying on a torus and therefore the boundary of the cell is not explicitly implemented. This approach presents the advantage of allowing the holes to exit the periodicity cell during the optimization process and to enter through the opposite face. Mesh variation and remeshing are necessary to accompany the variation of the cell. Section 5 describes the strategies used in the code to equilibrate, regularize and refine the mesh.

Section 6 is dedicated to numerical examples. Some technical details about the code are presented in the beginning of the Section while in subsection 6.1 information about the visualization routines is given. The examples of optimization problems for periodic microstructures presented in Section 7 in Part I [7] are analysed from the numerical point of view in subsections 6.2 through 6.6. In subsection 6.2 several examples are given for the maximization of the bulk modulus, for square and parallelogram periodicity cell, with one hole and with several holes. The optimization of homogenized coefficients is exemplified in subsection 6.3 while the maximization of the rigidity in a prescribed direction is presented in subsection 6.4. Subsection 6.5 deals with the maximization of rigidity for shear response when the periodicity cell is a square or a parallelogram. In subsection 6.6 a functional is used to minimize the Poisson coefficient, with the goal of obtaining auxetic materials.

Finally, in Section 7 some conclusions about the numerical method are pointed out.

2 Setting of the problem

Our goal is to optimize effective elastic properties of periodic porous microstructures, in two dimensions. The properties of the microstructure are described with the aid of the cellular problem

$$\begin{cases} -\operatorname{div}(\mathbf{C}\mathbf{e}(\mathbf{u}_A)) = \mathbf{0} \text{ in } \mathbb{R}_{\text{perf}}^2 \\ \mathbf{C}\mathbf{e}(\mathbf{u}_A)\mathbf{n} = \mathbf{0} \text{ on } \partial T \\ \mathbf{u}_A(\mathbf{x}) = \mathbf{A}\mathbf{x} + \phi_A(\mathbf{x}), \quad \phi_A \text{ periodic function} \end{cases} \quad (1)$$

where \mathbf{A} is a given effective strain (a symmetric 2×2 matrix), as explained in Sections 2 and 3 of Part I([7]). Recall that $\mathbb{R}_{\text{perf}}^2$ is the perforated plane

$$\mathbb{R}_{\text{perf}}^2 = \mathbb{R}^2 \setminus \bigcup_{\mathbf{k} \in \mathbb{Z}^2} (T + k_1 \mathbf{g}_1 + k_2 \mathbf{g}_2),$$

and the periodicity is described by a parallelogram cell Y defined by two vectors \mathbf{g}_1 and \mathbf{g}_2 . A model hole is denoted by T (see Figure 1).

For given effective strains \mathbf{A} and \mathbf{B} , one is looking for an effective material \mathbf{C}^H which minimizes the energy type quantity (see formula (13) in Part I [7])

$$\Phi = \langle \mathbf{C}^H \mathbf{A}, \mathbf{B} \rangle = \frac{1}{|Y|} \int_{Y \setminus T} \mathbf{C}\mathbf{e}(\mathbf{u}_A)\mathbf{e}(\mathbf{u}_B). \quad (2)$$

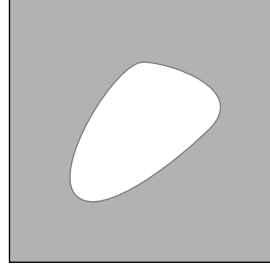


Fig. 1 Periodicity cell with model hole

For the base

$$\mathbf{f}_1 = \begin{bmatrix} 1 & 0 \\ 0 & 0 \end{bmatrix}, \quad \mathbf{f}_2 = \begin{bmatrix} 0 & 0 \\ 0 & 1 \end{bmatrix}, \quad \mathbf{f}_3 = \frac{1}{\sqrt{2}} \begin{bmatrix} 0 & 1 \\ 1 & 0 \end{bmatrix}$$

of symmetric 2×2 matrices, if $\mathbf{A} = a_i \mathbf{f}_i$ and $\mathbf{B} = b_j \mathbf{f}_j$, the functional to minimize (2) writes:

$$\Phi = a_i b_j \langle \mathbf{C}^H \mathbf{f}_i, \mathbf{f}_j \rangle = a_i b_j \frac{1}{|Y|} \int_{Y \setminus T} \mathbf{C}\mathbf{e}(\mathbf{u}_{f_i})\mathbf{e}(\mathbf{u}_{f_j}). \quad (3)$$

Here, \mathbf{u}_{f_i} is the solution of the problem

$$\begin{cases} -\operatorname{div}(\mathbf{C}\mathbf{e}(\mathbf{u}_{f_i})) = \mathbf{0} \text{ in } \mathbb{R}_{\text{perf}}^2 \\ \mathbf{C}\mathbf{e}(\mathbf{u}_{f_i})\mathbf{n} = \mathbf{0} \text{ on } \partial T \\ \mathbf{u}_{f_i}(\mathbf{x}) - \mathbf{f}_i \mathbf{x} \text{ is } Y\text{-periodic,} \end{cases} \quad (4)$$

for $i = 1, 2, 3$. Recall that the homogenized elastic tensor \mathbf{C}^H is completely characterized by

$$\mathbf{C}^H \mathbf{f}_i = \frac{1}{|Y|} \int_{Y \setminus T} \mathbf{C}\mathbf{e}(\mathbf{u}_{f_i}). \quad (5)$$

Note that these three problems are particular cases of the above problem (1), which is the same as (9) in Part I [7], for specific effective strains $\mathbf{A} = \mathbf{f}_i$.

With the goal of optimizing the effective properties of the microstructure, one minimizes a linear combination of energy type terms (3), which corresponds to minimizing a linear combination of homogenized (effective) elastic coefficients

$$\Phi = \alpha_{ij} \langle \mathbf{C}^H \mathbf{f}_i, \mathbf{f}_j \rangle = \alpha_{ij} \frac{1}{|Y|} \int_{Y \setminus T} \langle \mathbf{C}\mathbf{e}(\mathbf{u}_{f_i}), \mathbf{e}(\mathbf{u}_{f_j}) \rangle \quad (6)$$

where $\{\mathbf{f}_1, \mathbf{f}_2, \mathbf{f}_3\}$ is the above defined basis of symmetric matrices.

A constraint on the volume of material is considered. It is implemented through a penalization term of the form $\Lambda(V - V^*)^2$, where V denotes the volume percentage of the zone occupied by material:

$$V = \frac{|Y \setminus T|}{|Y|} = 1 - \frac{|T|}{|Y|},$$

$\Lambda > 0$ is a Lagrange multiplier and V^* is a ‘‘target’’ volume. The functional to minimize thus becomes

$$\Phi + \Lambda(V - V^*)^2 = \alpha_{ij} \langle \mathbf{C}^H \mathbf{f}_i, \mathbf{f}_j \rangle + \Lambda(V - V^*)^2 \quad (7)$$

(this is the so-called Lagrangean). Note that this approach does not guarantee that the final value of V be equal to the

“target” volume V^* ; one may adjust the values of Λ and of V^* in order to attain the desired volume fraction.

There is a more convenient approach where the user provides the desired volume fraction and the program finds the appropriate Lagrange multiplier Λ and then minimizes $\Phi + \Lambda V$. Although this can be done with no difficulty by simply introducing an iterative adapting process for Λ , the authors have chosen to minimize $\Phi + \Lambda(V - V^*)^2$ with Λ and V^* given since this “increases the convexity” of the functional and thus brings stability to the optimization process.

3 Optimization algorithm

Both shape and topological methods are based on the adjoint method. They share the same adjoint problem. Actually, they are self-adjoint. Therefore after solving the cellular problem one can directly compute the shape derivative and the topological derivative. So one has available the steepest descent direction for shape optimization if shape variations are desired and also the steepest descent direction for topological optimization if topology variation is desired.

The microstructure is represented in the computer through a triangular mesh on the periodicity cell Y . Some of the triangles are filled with elastic material C , others are considered to be void. The periodicity conditions are implicitly contained in the fact that the mesh is periodically closed in itself, therefore it has no boundary. This is equivalent to meshing the two-dimensional torus, see Section 4 for more details.

The algorithm starts with a given initial microstructure, and has the following layout:

Repeat Steps 1 and 2 until convergence:

1 Shape optimization

1.1 Solve the cellular problem (4)

1.2 Compute the shape derivative

1.3 Deform the geometry in accordance to the shape derivative

2 Topology optimization

2.1 Solve the cellular problem (4)

2.2 Compute the topological derivative

2.3 Change the topology following the topological derivative

Steps 1.1 and 2.1 are identical, and consist in solving the three cellular problems (4). As explained in Section 2, this produces three cellular solutions \mathbf{u}_{f_1} , \mathbf{u}_{f_2} and \mathbf{u}_{f_3} . In particular, this allows for the computation of the homogenized elastic tensor C^H through formula (5). The computation of the cellular solutions is based on the finite element method which is described in some detail in Section 4.

The computation of the shape derivative of the functional $\Phi + \Lambda(V - V^*)^2$ in (7), performed in Step 1.2, is based on Theorem 5 in Part I [7] for the energy terms (6)

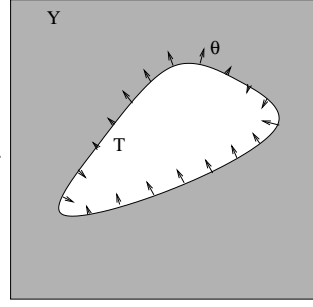


Fig. 2 Deformation speed θ

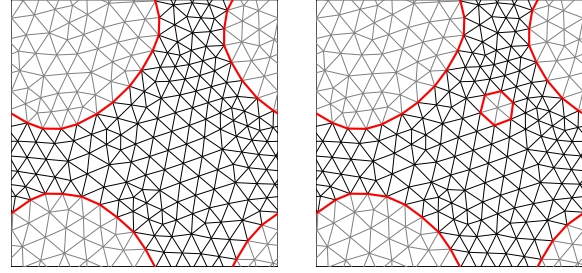


Fig. 3 Nucleation of a new hole

and on formula (34) in Part I [7] for the volume percentage V . Thus, the shape derivative of the Lagrangean has the form

$$D_S(\Phi + \Lambda(V - V^*)^2) = \int_{\partial T} \gamma \theta \cdot \mathbf{n} \quad (8)$$

where

$$\gamma = \frac{1}{|Y|} \left[\alpha_{ij} (2\mu \langle \mathbf{e}(\mathbf{u}_{f_i}), \mathbf{e}(\mathbf{u}_{f_j}) \rangle + \lambda \text{tr} \mathbf{e}(\mathbf{u}_{f_i}) \text{tr} \mathbf{e}(\mathbf{u}_{f_j})) + 2\Lambda(V - V^*) \right]$$

is a scalar function defined on ∂T and depending on the Lamé coefficients of the material λ and μ , on the solutions \mathbf{u}_{f_i} , on the Lagrange multiplier Λ and on the “target” volume V^* .

The deformation of the shape (Step 1.3) is done by moving the boundary of the hole ∂T in a direction θ which ensure that the value of Φ decreases. This is accomplished by choosing $\theta = -\gamma \mathbf{n}$, see Figure 2. Section 5 describes in some detail the deformation of the mesh and the subsequent remeshing procedure.

Step 2.2 computes the topological derivative of the Lagrangean (7) and is based on Theorem 4 in Part I [7] for the energy terms and on formula (30) in Part I [7] for the volume term. The expression of the topological derivative is

$$D_T(\Phi + \Lambda(V - V^*)^2) = -\alpha_{ij} \frac{\pi}{|Y|} \frac{\lambda + 2\mu}{\lambda + \mu} \left[4\mu \mathbf{e}(\mathbf{u}_{f_i}) \mathbf{e}(\mathbf{u}_{f_j}) + \frac{\lambda^2 + 2\lambda\mu - \mu^2}{\mu} \text{tr} \mathbf{e}(\mathbf{u}_{f_i}) \text{tr} \mathbf{e}(\mathbf{u}_{f_j}) \right] - 2\Lambda(V - V^*) \frac{\pi}{|Y|},$$

Step 2.3 introduces holes at points where the topological derivative (computed at Step 2.2) has negative minima. This

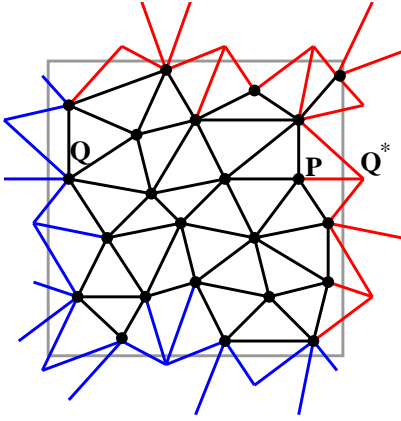


Fig. 4 Finite element mesh

is done by simply changing the triangles in the neighbourhood of the respective node from material to void, see Figure 3.

4 Finite elements for periodic elliptic problems

When solving the cellular problem (1), it makes no sense to discretize the whole $\mathbb{R}^2_{\text{perf}}$. One should discretize a representative region, for instance the periodicity cell Y , and ensure the linear+periodic character of the solution \mathbf{u}_A .

The approach used in the present paper (proposed in [5] and [6]) consists of meshing the cell Y and implementing the periodicity conditions by giving a special treatment to segments which cross the boundary of Y . In fact the mesh lives on the two-dimensional torus. For visualization purposes, Figure 4 shows the unfolded mesh where each segment which crosses the boundary is drawn twice, in red and in blue. However, only one instance of the segment actually exists in the code (the red one). The boundary of the cell Y is not explicitly implemented. It is defined implicitly through the segments crossing it. From the differential geometry viewpoint, the segments crossing the boundary mark the entrance into the next foil on the torus.

A unified treatment is given to all segments (interior or crossing the boundary). In the optimization process, when the mesh evolves, this approach allows us to handle in the same way the segments which initially were crossing the boundary and the interior ones. This is especially important in examples where a hole extends over several periodicity cells. Figure 5 presents such a case, which corresponds to the microstructure shown in Figure 6.

This is done by associating to each segment a pair of flags (integer numbers) $flag_1$ and $flag_2$. For most of the segments (drawn in black in Figure 4), the flags are $(0,0)$, which means they need no special treatment. The segments crossing the right boundary of the cell Y have the flag $(1,0)$ while those crossing the upper boundary of the cell Y have the flag

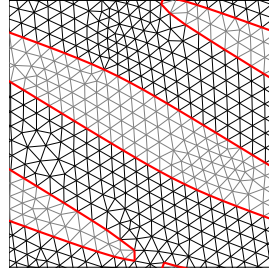


Fig. 5 Hole crossing the boundary of the cell

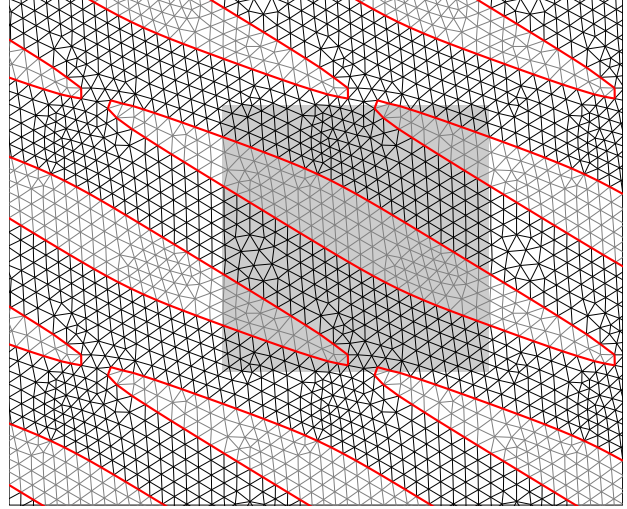


Fig. 6 Unfolded mesh

$(0,1)$. Only two segments, located in the upper right corner, have flag of $(1,1)$. Note that the blue segments (crossing the left or lower boundaries of Y) do not exist in our approach since we deal with the unfolded mesh from the torus.

The *flag* variable is the main ingredient in the implementation of the periodicity conditions.

For instance, the nodes \mathbf{P} and \mathbf{Q} in the unfolded mesh in Figure 4 are neighbours in the mesh on the torus. The coordinates of the segment pointing from \mathbf{P} to \mathbf{Q} are

$$(Q_1 - P_1 + flag_1, Q_2 - P_2 + flag_2)$$

(considering the periodicity cell Y to be the unit square). Note that only if the flag of the segment is $(0,0)$ then its coordinates are the expected ones: $(Q_1 - P_1, Q_2 - P_2)$. Note also that node \mathbf{Q}^* does not exist in the code, it is drawn only for visualization purposes.

For a rectangular cell of sides h_1 and h_2 , the coordinates of a segment pointing from \mathbf{P} to \mathbf{Q} can be expressed as

$$(Q_1 - P_1 + flag_1 h_1, Q_2 - P_2 + flag_2 h_2).$$

In the general case when the periodicity cell is a parallelogram defined by vectors \mathbf{g}_1 and \mathbf{g}_2 , a segment pointing from node \mathbf{P} to node \mathbf{Q} can be identified with the vector

$$\mathbf{Q} - \mathbf{P} + flag_1 \mathbf{g}_1 + flag_2 \mathbf{g}_2.$$

We shall consider Lagrange P1 finite elements, that is, functions which are affine on each triangle of the mesh (while globally continuous). Since the mesh is periodically closed (lives on the torus), a periodic function can be implemented by simply storing its values in the nodes. This is no longer true for linear+periodic functions.

Linear+periodic functions are implemented by storing their values in each node of the mesh, and by additionally storing the matrix A which describes the linear part of the function:

$$\mathbf{u}_A = A\mathbf{x} + \phi_A(\mathbf{x}),$$

see the definition of the space LP in [7], Section 2, and also the definition of the space LP_{perf} in [7], Section 4.

Through the finite element technique, the cellular problem is transformed into a discretized elliptic problem which is a linear system of equations whose unknowns are the values of the function \mathbf{u}_A in every node \mathbf{P} of the mesh. Each of these linear equations relate the value of \mathbf{u}_A in the current node \mathbf{P} with the values of \mathbf{u}_A in its neighbour nodes. For the particular case of segments crossing the boundary of the cell Y (see Figure 4), the value of the function \mathbf{u}_A in the virtual node \mathbf{Q}^* is obtained through the formula

$$\mathbf{u}_A(\mathbf{Q}^*) = \mathbf{u}_A(\mathbf{Q}) + \text{flag}_1 A\mathbf{g}_1 + \text{flag}_2 A\mathbf{g}_2.$$

Here, $(\text{flag}_1, \text{flag}_2)$ are the flags associated to the segment pointing from node \mathbf{P} to node \mathbf{Q} and $\mathbf{g}_1, \mathbf{g}_2$ are the vectors defining the periodicity parallelogram Y .

5 Mesh variation and remeshing

Step 1.3 in the optimization algorithm (described in Section 3) consists of deforming the shape of the hole(s) defining the microstructure, according to the shape derivative computed at Step 1.2. The shape derivative is a scalar function defined on the boundary of the hole(s). It gives a descent direction for minimizing the Lagrangean (7), more precisely, it suggests a deformation velocity field of $-\gamma\mathbf{n}$, where γ is the integrand in the shape derivative formula (8). Since this vector field is defined only on the boundary of the hole(s) ∂T , the first task is to extend it to the whole domain Y in order to subsequently apply a global deformation. This extension operation is done by initializing the vector field with the value zero at all nodes not belonging to ∂T ; then, the value of the velocity at each such node is replaced by the average of the velocities of its neighbours. By performing this average operation several times, the computed values of the velocity field on the boundary of the hole(s) steadily propagate to all nodes of the mesh.

The deformation is then applied to the entire mesh (more precisely, to all nodes). Because of the averaging process above described, the deformation is quite smooth and the

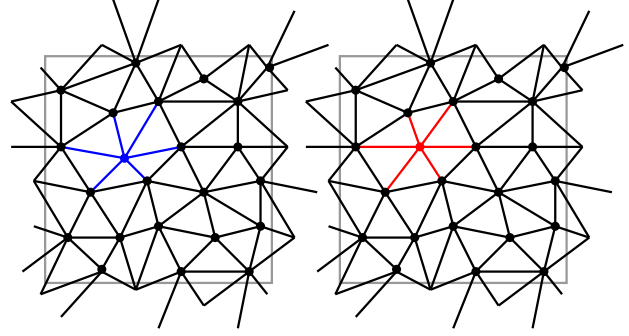


Fig. 7 Mesh before and after baricenter operation

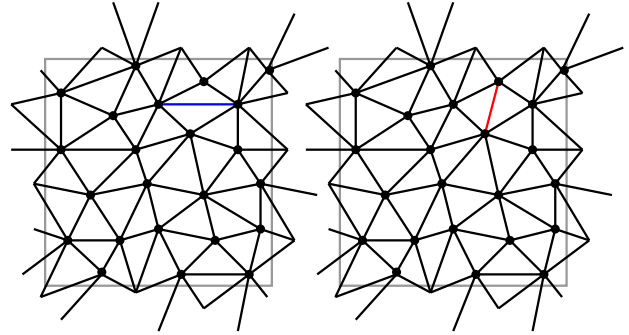


Fig. 8 Mesh before and after flip operation

deformed mesh keeps its regularity properties for a reasonable number of deformation steps.

However, the quality of the mesh eventually decays: sharp angles appear, or large differences in the size of the segments show up. The authors have chosen not to remesh from scratch, but instead to improve frequently the quality of the mesh, either by moving the nodes (equilibrating the mesh) or by changing the elements of the mesh (flipping segments, adding/eliminating nodes).

The mesh is equilibrated in the following way: each node is moved from its current position to the baricenter of its neighbour nodes, see Figure 7. This procedure is applied to the whole mesh and is repeated several times until equilibrium is attained. In order to keep the shape of the hole(s) unchanged, nodes on the boundary of the hole(s) are not equilibrated.

In order to avoid too sharp angles in the triangles of the mesh, flipping is performed on those segments opposite to wide angles, see Figure 8. Neighbour angles are measured before and after the flip, and the more convenient configuration is retained. Again, in order to maintain the shape of the hole(s), this operation is not performed on segments belonging to the boundary of the hole(s).

The two operations described above (baricenters and flips) are performed alternatively to ensure the stability of the mesh.

Baricenters and flips provide some flexibility to the mesh but in certain situations the deformation is too large and it turns out that one must eliminate nodes from some zones of the domain and/or insert new nodes in other zones.

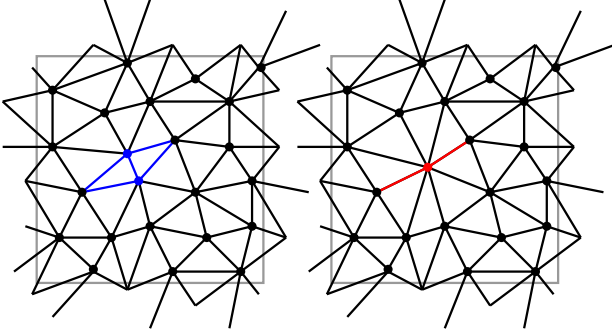


Fig. 9 Mesh before and after elimination of one segment

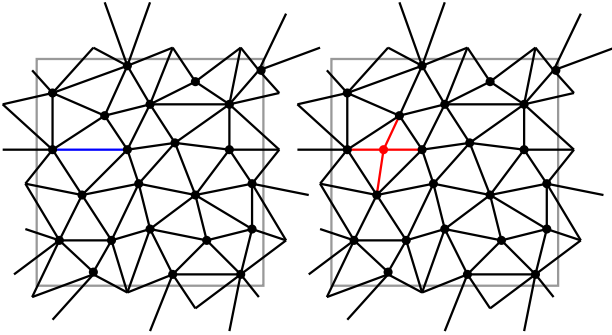


Fig. 10 Mesh before and after insertion of one node

Supposing that the desired mesh has a characteristic segment length ℓ , the global strategy of remeshing relies on the following two operations: elimination of segments shorter than $(1 - \delta)\ell$ (see Figure 9) and insertion of a new node in the middle of segments longer than $(1 + \delta)\ell$ (see Figure 10). Here, δ is a small parameter, usually taken as $\delta = 0.2$. This is performed from time to time, with decreasing characteristic length ℓ in order to obtain a refined and equilibrated mesh.

There is a case which needs special treatment: when two holes are very close to each other, the remeshing routine may try to eliminate a segment touching both holes. When this happens, the neighbour triangles are changed into void triangles, thus allowing for the two holes to merge.

6 Numerical examples

In the present section, several examples of optimizing porous microstructures are presented. The results were computed by a FORTRAN code programmed by the authors, which uses parts of the code described in [5] and [6].

Void inclusions are considered in a matrix of isotropic elastic material whose elastic tensor is $C\xi = 2\mu\xi + \lambda(\text{tr}\xi)I$, for Lamé coefficients $\lambda = 3$ and $\mu = 1$ (see Remark 7 in Part I [7]).

Note that, for an arbitrary microstructure, although C is isotropic, there is no reason for C^H to be isotropic. For microstructures having square symmetry, the homogenized

elastic tensor C^H is orthotropic. For microstructures having hexagonal symmetry (like the ones presented in Figure 13), C^H is isotropic. See [10] for more details.

6.1 Graphical routines

The microstructures are represented graphically by simply drawing the triangular mesh used to discretize the domain. Full material is represented by bold segments, while the region occupied by the void is represented using thinner segments. Note that we mesh the void region, although these triangles are not used in the finite element analysis. The interface (the boundary of the hole) is drawn in red.

The case of two (or more) different materials, with holes or with no hole, is implemented in the code. However, the results presented here are about mixtures between one material and void only.

It should be stressed that the Figures in this Section show several contiguous periodicity cells, in order to provide a global image of the porous microstructure. In some Figures a grey parallelogram is drawn, representing the periodicity cell Y . However, the finite element analysis and the optimization procedure are performed on one cell only, as explained in Section 4.

The drawings are produced by a Python script which reads the mesh (saved from FORTRAN) and writes out directly PostScript code. An interactive interface was programmed in Python in order to produce animations (see the web page <http://cmaf.ptmat.fc.ul.pt/~barbaros/en/optper/> for an example).

6.2 Maximization of the bulk modulus

The series of examples begins with the maximization of the bulk modulus of the homogenized elastic tensor C^H . Define the matrix

$$A = \begin{bmatrix} -1 & 0 \\ 0 & -1 \end{bmatrix},$$

which represents a pure compression strain, and maximize

$$\langle C^H A, A \rangle = C_{1111}^H + 2C_{1122}^H + C_{2222}^H. \quad (9)$$

This is equivalent to minimizing

$$\Phi = -\langle C^H A, A \rangle = -C_{1111}^H - 2C_{1122}^H - C_{2222}^H.$$

A first case is considered, with square periodicity cell and one hole only. The optimization algorithm is applied, with no topology optimization, that is, shape optimization only is performed. In Figure 11, an initial mesh is presented on the left. It contains a small initial hole at an arbitrary location. A volume constraint $V^* = 61\%$ is considered. After 400 minimization steps, one obtains the mesh presented in

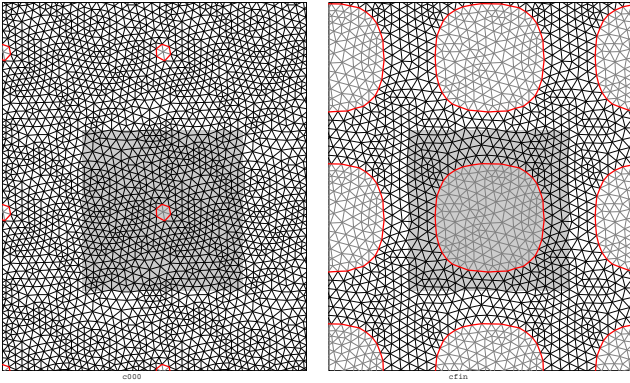


Fig. 11 Maximization of the bulk modulus

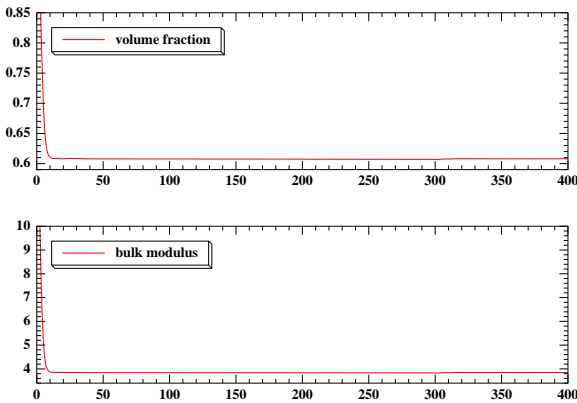


Fig. 12 History of convergence

Figure 11 on the right. Note that the mesh changes a lot, especially inside the hole and along its boundary. The shape of the final hole is very similar to the so-called Vigdergauz structure, see [16].

The evolution of the volume fraction and of the energy $\langle C^H A, A \rangle$ are presented in Figure 12. The final mesh has 346 vertices.

Next, a parallelogram periodicity cell is tested, more precisely, a 60° rhombus cell, still for the maximization of (9), with one hole only. A low target volume was chosen (28%) in order to show the appearance of a honeycomb structure. Results are shown in Figure 13 : initial guess, design after one iteration, after 8 iterations and at the end of the process (after 400 iterations). The final microstructure has a volume fraction of 30% and a bulk modulus of 1.233. Note that this final structure is obtained with one hole only in the periodicity cell Y , but this hole cannot be confined to the interior of the cell: it exists partially and enters the opposite side of Y . This possibility was described from a theoretical point of view in Remark 8 in Part I [7]. This example recovers the result presented in [6], Figure 11, with obvious mesh improvement. Note also that in [6] the initial hole should have a volume close to the target volume. In contrast, in the present work the initial hole is very small (see first mesh

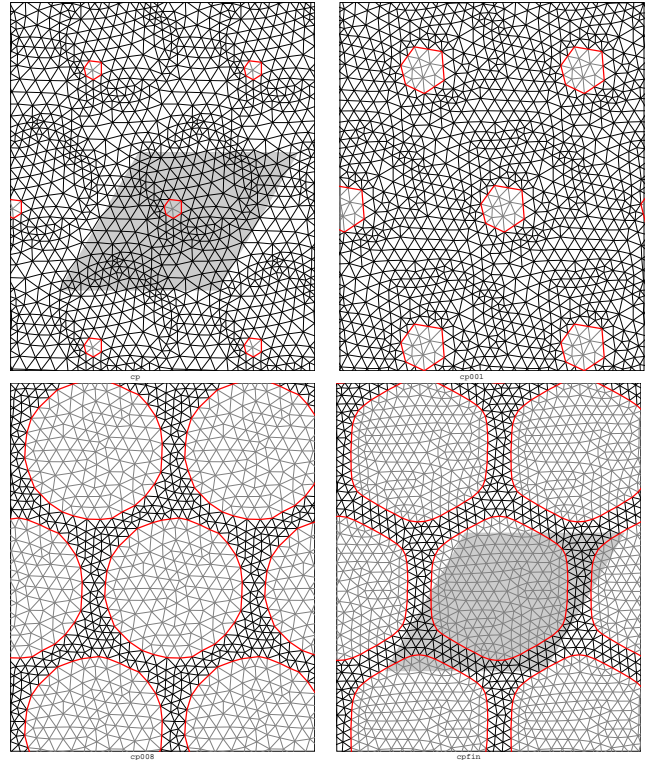


Fig. 13 Maximization of the bulk modulus – rhombic cell

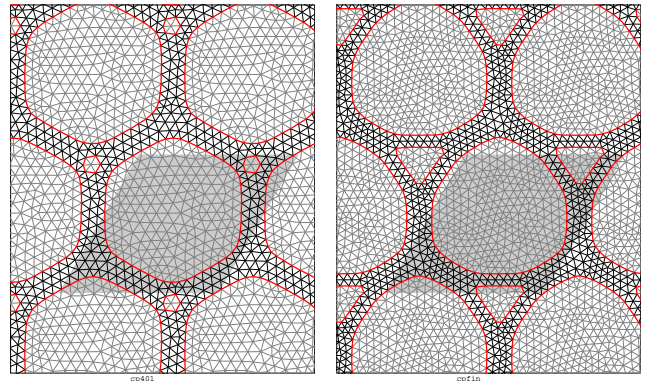


Fig. 14 Rhombic cell – nucleation of a hole at iteration 401 and final design.

in Figure 13) and varies a lot during the shape optimization process.

The process illustrated in Figure 13 was continued by introducing one topology optimization step followed by 200 iterations of shape optimization. Figure 14 shows the mesh immediately after the hole nucleation, after 36 shape optimization steps and the final mesh after 200 shape optimization steps. We obtain the same volume fraction 30% and roughly the same bulk modulus 1.226.

Figures 15 to 22 illustrate a long process of alternate application of shape optimization and topology optimization, for the same parallelogram periodicity cell. The “target” volume is 56%. One can see new holes appearing and

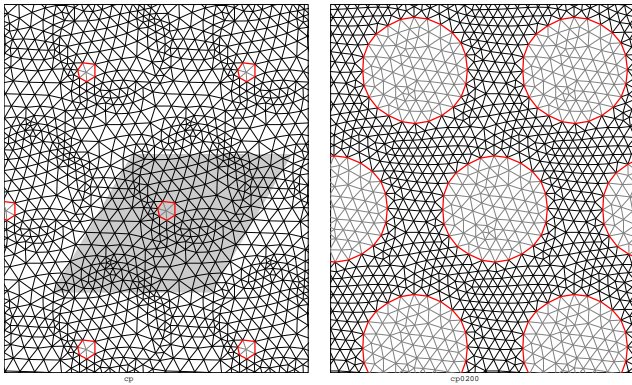


Fig. 15 Maximization of the bulk modulus – rhombic cell. Initial guess and iteration 200.

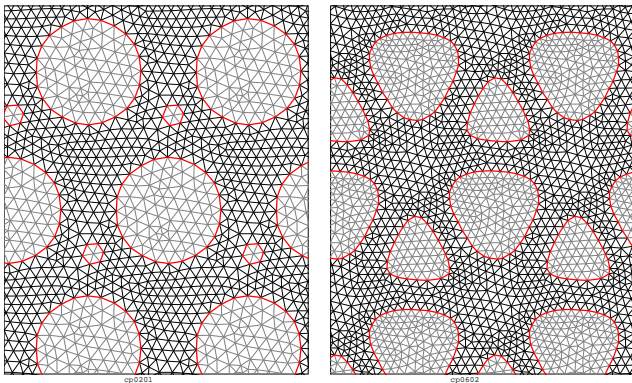


Fig. 16 Maximization of the bulk modulus – rhombic cell. Nucleation of hole at iteration 201 and iteration 602.

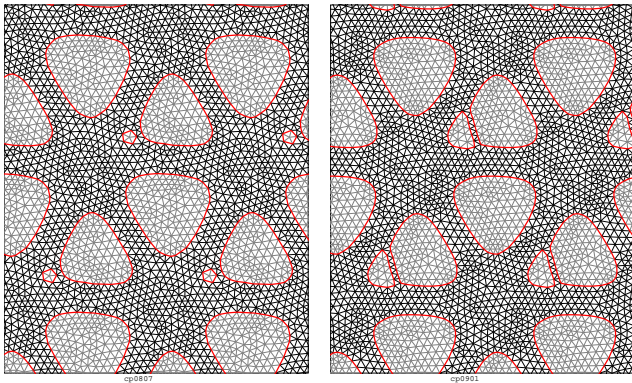


Fig. 17 Maximization of the bulk modulus – rhombic cell. Nucleation of hole at iteration 807 and iteration 901.

eventually merging with previous holes. This happens several times. As it can be seen from the history of convergence in Figure 22, the objective functional and the volume fraction are almost constant, except for the first few iterations. This suggests that the problem of maximizing the bulk modulus has more than one solution, maybe an infinite number of solutions. The small oscillations appearing in the convergence history correspond to changes in the parameter that controls the characteristic size of the mesh. Immediately after mesh refinement the functional increases but decreases af-

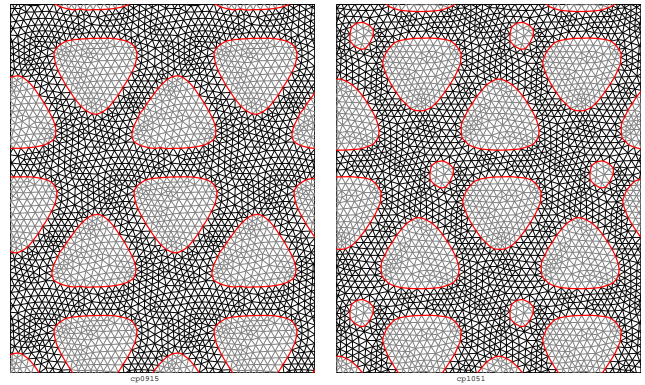


Fig. 18 Maximization of the bulk modulus – rhombic cell. Merging of holes at iteration 915 and iteration 1051 after nucleation of hole.

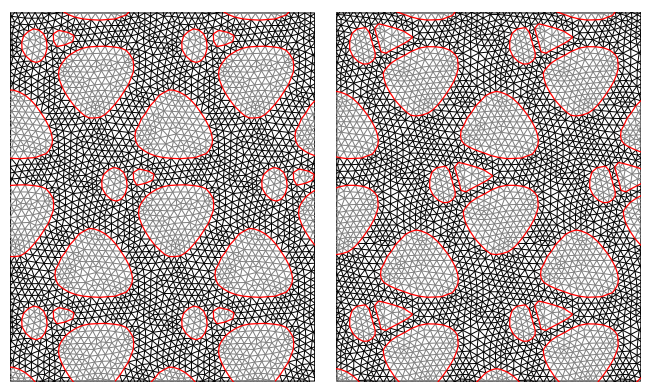


Fig. 19 Maximization of the bulk modulus – rhombic cell. Iteration 1117 and iteration 1161 : after nucleation of holes.

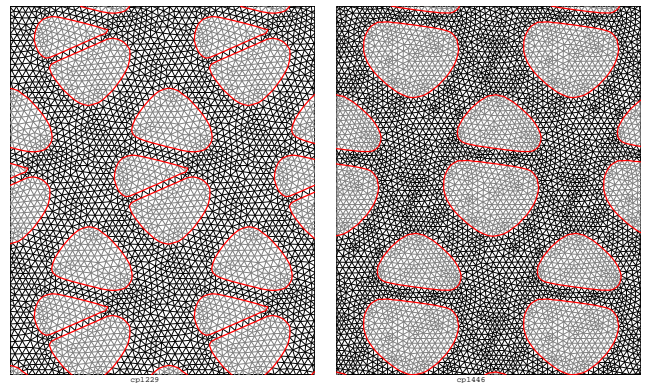


Fig. 20 Maximization of the bulk modulus – rhombic cell. Iteration 1229 and iteration 1446 : merging of holes.

ter the equilibrating the mesh. Note that in the final design (Figure 21) the mesh is quite regular.

6.3 Optimization of homogenized coefficients

An important example is to maximize the homogenized coefficients.

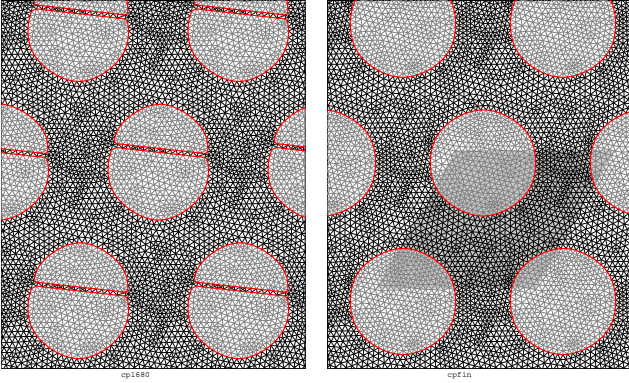


Fig. 21 Maximization of the bulk modulus – rhombic cell. Iteration 1680 and iteration 1900 : final design

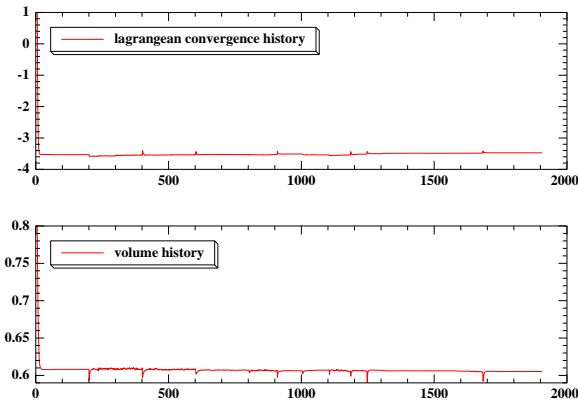


Fig. 22 Rhombic cell – history of convergence

For instance the maximization of the homogenized coefficient C_{1111}^H is obtained by considering the effective strain matrix

$$A = \begin{bmatrix} 1 & 0 \\ 0 & 0 \end{bmatrix}.$$

Then the functional to maximize writes

$$\langle C^H A, A \rangle = C_{1111}^H. \quad (10)$$

For a square periodicity cell, taking the Lagrange multiplier $\Lambda = 150$ and the “target” volume of $V^* = 56\%$, the obtained results are shown in Figure 23. Shape optimization only is applied. The initial guess has a small hole which evolves rapidly (see iteration 26 in Figure 23) and assumes a horizontal orientation (see iteration 110 in Figure 23). In the final design, obtained after 142 iterations, the hole tries to merge to itself (recall that the mesh lives on a torus). Note that the code allows the holes to merge; however, in this example the process was stopped immediately before the merging operation, in order to avoid the degeneration of the homogenized elastic tensor. The numerical results agree with the expected ones : the optimal design for the maximization of the homogenized coefficient C_{1111}^H is a laminate. The corresponding periodicity cell is made of horizon-

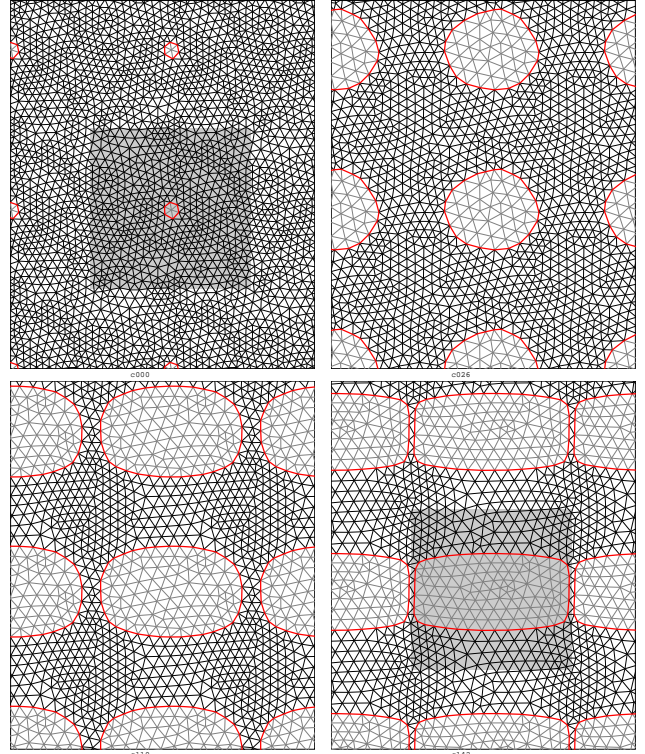


Fig. 23 Maximization of C_{1111}^H : initial guess, iteration 26, iteration 110 and final design (iteration 142).

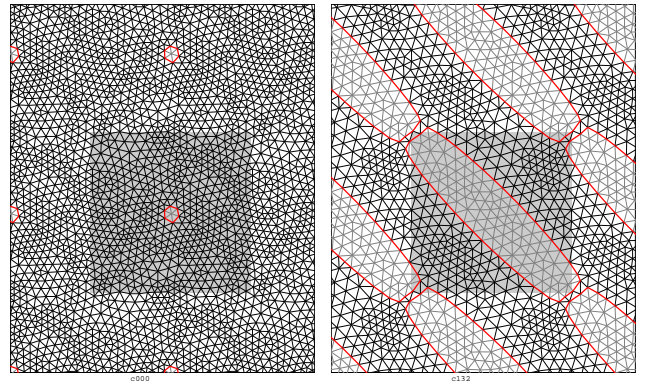


Fig. 24 Maximization of rigidity in the second bisector direction $(-1, 1)$: initial guess and final design (iteration 132).

tal bands of material, of thickness defined by the desired volume.

6.4 Maximization of rigidity in a prescribed direction

When one tries to maximize the rigidity of an elastic microstructure to a compression load in a certain direction of the space, the theoretical optimum is attained by rank one laminates parallel to the prescribed direction, see e.g. [4] or Section 2.3 in [2].

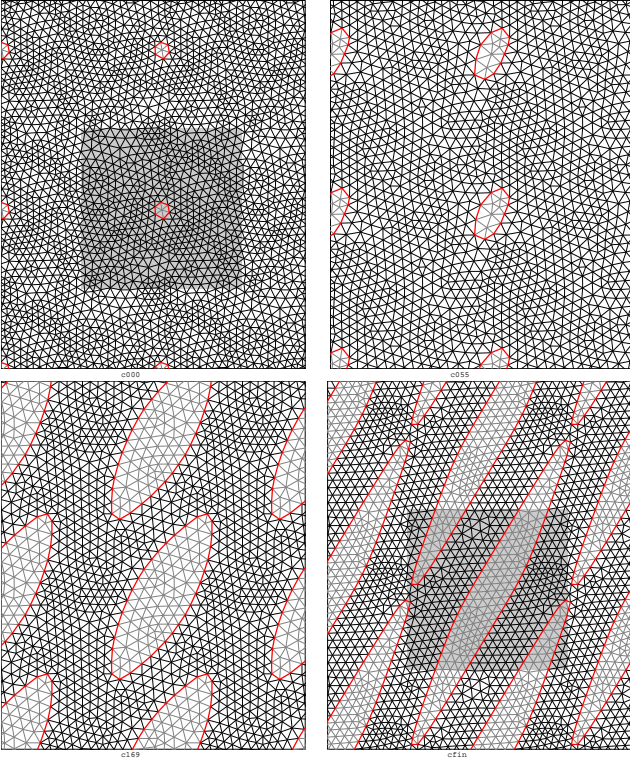


Fig. 25 Maximization of rigidity in the direction (1,2): initial guess, iterations 55, 169 and final design (iteration 900)

Consider a square periodicity cell and an effective strain matrix

$$A = \begin{bmatrix} -1 & 1 \\ 1 & -1 \end{bmatrix},$$

which corresponds to a compression load in the direction of the second bisector of the plane (-1,1). The functional to maximize is then

$$\langle C^H A, A \rangle = C_{1111}^H + C_{1212}^H + C_{2222}^H + 2C_{1122}^H - 2C_{1112}^H - 2C_{1222}^H$$

and it corresponds to maximization of rigidity in the direction (-1, 1). The numerical results (see Figure 24) were obtained for a Lagrange multiplier $\Lambda = 150$ and the “target” volume $V^* = 56\%$. The initial guess is a periodicity cell with a small hole. Shape optimization only is performed. The final design presents a hole that exits the periodicity cell and enters on its opposite side as announced in Section 4. Note that it is possible to obtain such an example since the mesh lies on a torus and the hole has total freedom of movement with respect to the periodicity cell.

Another example is shown in Figure 25 for the maximization of the rigidity in the direction (1,2). This is done by choosing an effective strain matrix

$$A = \begin{bmatrix} 1 & 2 \\ 2 & 4 \end{bmatrix}.$$

The functional to maximize writes :

$$\langle C^H A, A \rangle = C_{1111}^H + 4C_{1212}^H + 16C_{2222}^H + 4C_{1112}^H + 8C_{1122}^H + 16C_{1222}^H$$

The initial guess is the same as in the previous example. In Figure 25 one can see how the hole becomes very elongated and in the end it makes a double loop on the torus. Again, the process has to be stopped before the hole touches itself and the cellular problem degenerates.

In the example in Figure 25, topology optimization is alternated with shape optimization. However, due to the particular form of the functional Φ , each topology optimization step adds a small hole *contiguous* to the existing hole, precisely at one of its extremities. Thus, the only effect of topology optimization is to accelerate the elongation of the hole in the prescribed direction (1,2).

6.5 Maximization of rigidity for shear response

This subsection presents two examples of maximization of the response of a microstructure to shear. Define the effective strain matrix

$$A = \begin{bmatrix} 0 & 1 \\ 1 & 0 \end{bmatrix}$$

which corresponds to pure shear strain, and maximize the functional

$$\langle C^H A, A \rangle = 4C_{1212}^H.$$

In Figure 26, a square periodicity cell is considered. The volume constraint is given by parameters $\Lambda = 150$, $V^* = 56\%$. Initially, the shape optimization algorithm tries to find the best structure with one hole only. Then, at iteration 31, a new hole is nucleated changing the topology. Afterwards, at every 50 iterations of shape optimization, topology optimization is performed and the characteristic length of the mesh is decreased. However one observes no variation in the topology : either the new introduced holes merge to the existing ones, contributing to the shape variation, or no hole at all is nucleated because the topology derivative is everywhere positive. The history of the volume and the values of C_{1212}^H are presented in Figure 27. The volume of the final design is 57,31% and the coefficient $C_{1212}^H = 0.477$. This example shows similar results to those obtained in [6] (Figure 23) only with shape optimization and with an initial guess with two holes.

In Figure 28, a rhombic periodicity cell is considered. The initial guess is a cell with a small hole. Shape optimization is performed and at iteration 31 a new hole is nucleated by the topology optimization process. The new hole merges with the existing one so no variation of topology occurs. The optimization process continues with shape optimization only although every 50 iterations the code tests for topology

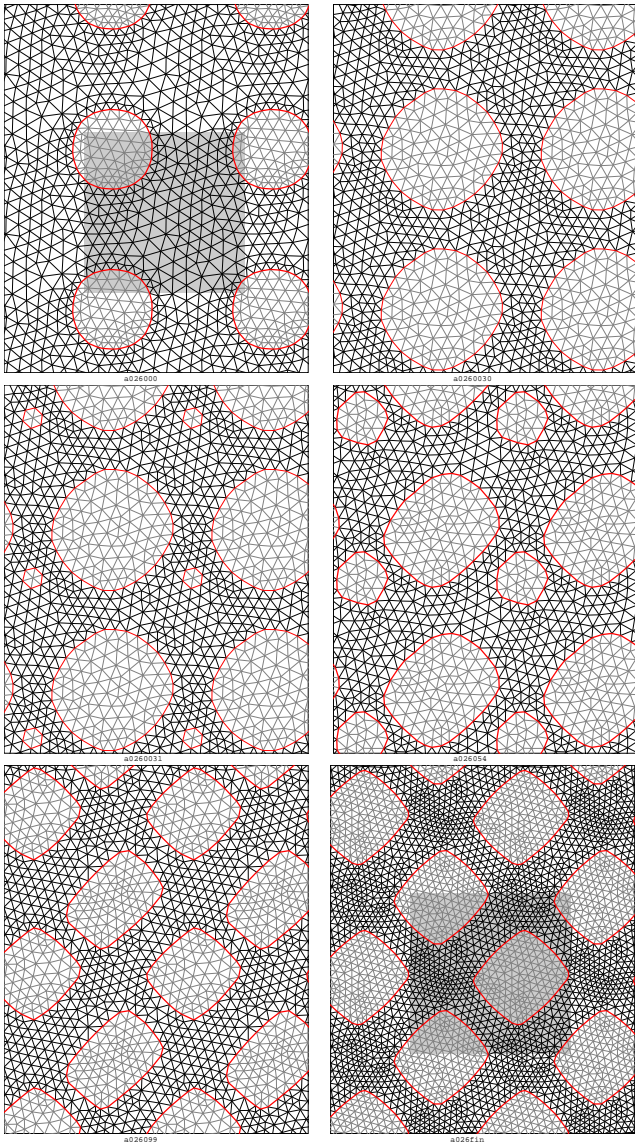


Fig. 26 Maximizing the response to shear : initial guess, iterations 30, 31, 54, 99 and 482 (final design).

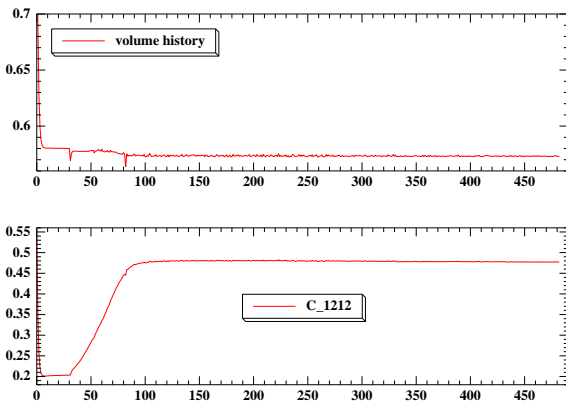


Fig. 27 Maximizing the response to shear with square periodicity cell: history of volume fraction and of C_{1212}^H .

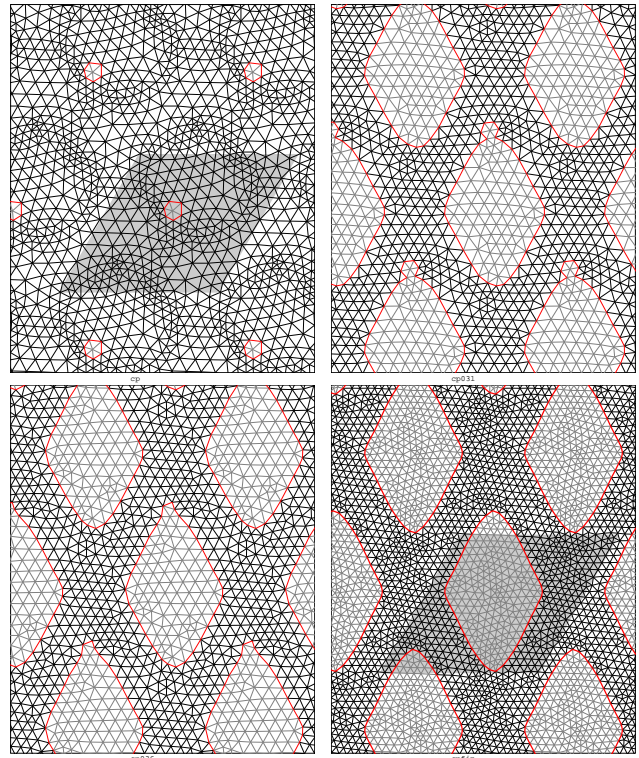


Fig. 28 Maximizing the response to shear – parallelogram cell : initial guess, iteration 31, 36 and 481 (final design).

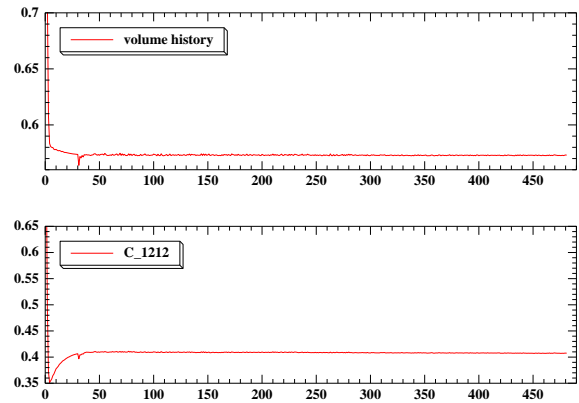


Fig. 29 Maximizing the response to shear with rhombic periodicity cell : history of volume fraction and of C_{1212}^H .

variation. The volume of the final design, 57,29% is very close to the one obtained with a square cell in the previous example, however the coefficient $C_{1212}^H = 0.4075$ is smaller.

These two examples show that by optimizing with a different periodicity cell, one may obtain a different optimal value of the cost functional.

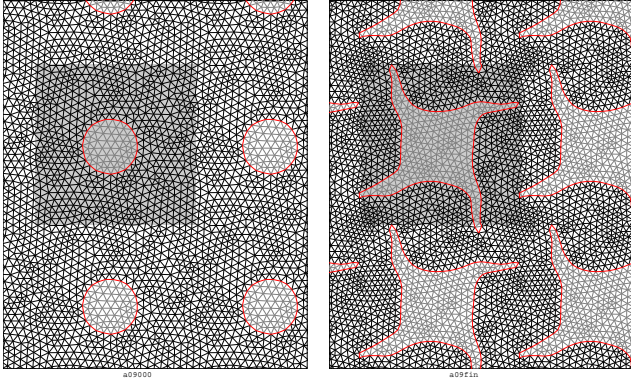


Fig. 30 Minimization of the Poisson coefficient with one hole : initial guess and final design (iteration 120).

6.6 Minimization of the Poisson coefficient

With the goal of obtaining auxetic materials, one searches for a homogenized tensor C^H having a negative Poisson coefficient. For an anisotropic elastic tensor C^H , the behaviour of the microstructure is characterized through two Poisson-like coefficients defined by:

$$-\frac{D_{2211}^H}{D_{1111}^H} \quad \text{or} \quad -\frac{D_{2211}^H}{D_{2222}^H}$$

where D^H is the inverse tensor of C^H . However, in order to avoid computing the derivative of the above fraction, a different approach is considered: defining the two effective strains

$$A = \begin{bmatrix} 1 & 0 \\ 0 & 0 \end{bmatrix}, \quad B = \begin{bmatrix} 0 & 0 \\ 0 & 1 \end{bmatrix}$$

minimize

$$\langle C^H A, B \rangle = C_{1122}^H$$

This is of course not equivalent to minimizing the Poisson coefficient itself, but it goes in the right direction.

The optimization algorithm was tested with a square periodicity cell, starting with a initial guess having one, two and three holes, respectively. No topology optimization is performed, but only shape optimization. When tested with topology optimization, instabilities appear because holes are nucleated contiguous to the existing ones, at their extremities.

In these examples, no volume constraint was considered that is the Lagrange multiplier is set to 0.

Figure 30 presents the initial guess and the final design obtained for one hole. The volume starts at 90.8% and decreases down to 70.9% in the final design. The homogenized coefficient C_{1122}^H reaches negative values (see Figure 31). However the Poisson-like coefficients remain both positive :

$$-\frac{D_{2211}^H}{D_{1111}^H} = 0.11 \quad \text{and} \quad -\frac{D_{2211}^H}{D_{2222}^H} = 0.13.$$

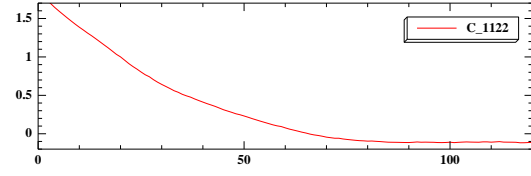


Fig. 31 Minimization of the Poisson coefficient with one hole : history of C_{1122}^H

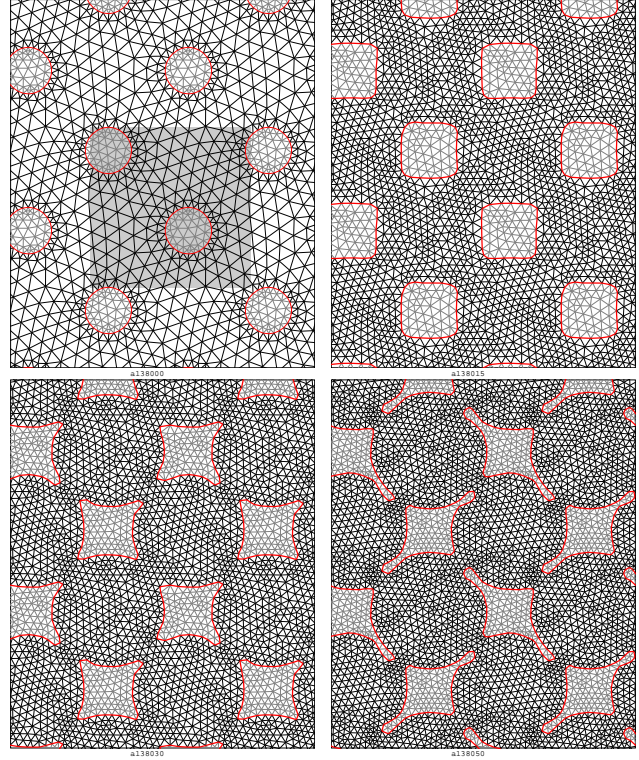


Fig. 32 Minimization of the Poisson coefficient with two holes : initial guess, iterations 15, 30 and 50.

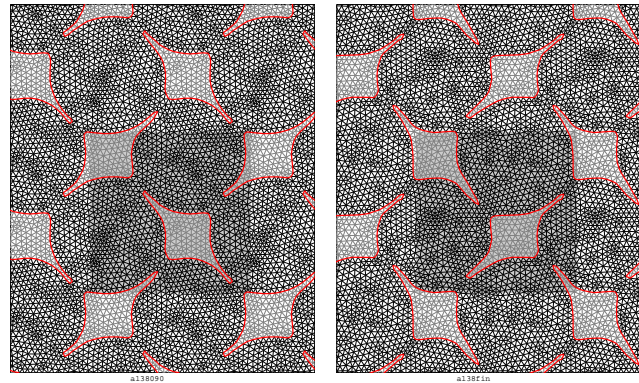


Fig. 33 Minimization of the Poisson coefficient with two holes : final design (iteration 90) and symmetric geometry.

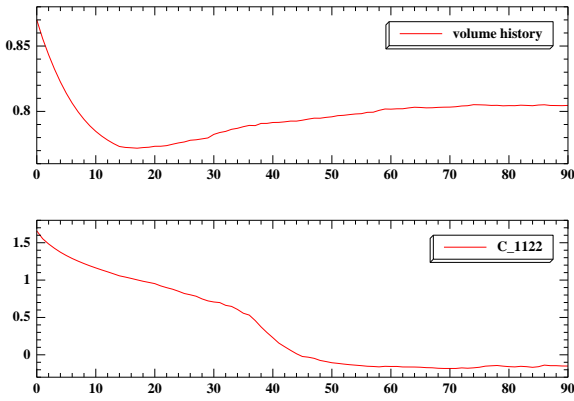


Fig. 34 Minimization of the Poisson coefficient with two holes : history of C_{1122}^H and of the volume fraction.

Note that for the initial guess both Poisson-like coefficients are equal to 0.52.

Figures 32 and 33 present the same optimization process but with two holes. Note that two different optimization processes are represented. The initial guess, iterations 15, 30 and 50 in Figure 32 and the final design (left picture in Figure 33) correspond to the first process, as well as the convergence history graphs in Figure 34. The righthand picture in Figure 33 is the final design resulting from the second optimization process. The two processes differ only in the initialization of the value of the cellular solution in the newly created vertex after each split operation. Although this represents a very slight difference, since the final geometry is not symmetric, the code finds the reverse configuration.

The microstructures represented in the lefthand picture in Figure 33, on a mesh with 1125 nodes, has negative Poisson-like coefficients,

$$-\frac{D_{2211}^H}{D_{1111}^H} = -0.27 \quad \text{and} \quad -\frac{D_{2211}^H}{D_{2222}^H} = -0.24,$$

while the volume stabilises at 80%. The initial guess had a volume of 87% and both Poisson-like coefficients equal to 0.53. The run time for each example was almost 12 minutes on a processor Pentium 4 with 2.8 GHz.

Starting with an initial guess with 5 small holes (see Figure 35), of volume 96 % and Poisson-like coefficients 0.56), two pairs of holes merge during the optimization process (see iterations 10 and 20 in Figure 35) and the design stabilises in the class of periodicity cells with three holes (see the final design). The Poisson-like coefficients of the final design are

$$-\frac{D_{2211}^H}{D_{1111}^H} = -0.18 \quad \text{and} \quad -\frac{D_{2211}^H}{D_{2222}^H} = -0.20,$$

for a volume of 78 %. The history of the volume and the evolution of the coefficient C_{1122}^H are represented in Figure 36.

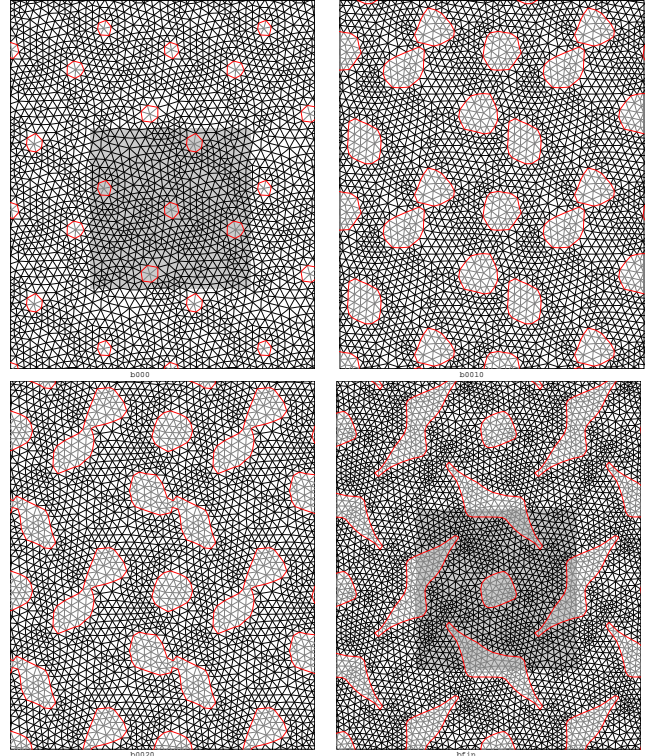


Fig. 35 Minimization of the Poisson coefficient with three holes : initial guess, iterations 10, 20 and final design (iteration 120).

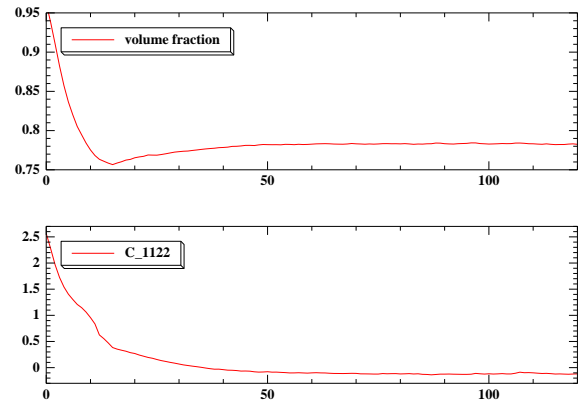


Fig. 36 Minimization of the Poisson coefficient with three holes : history of C_{1122}^H and of the volume fraction.

7 Conclusions

An optimization algorithm is described for the design of periodic porous materials. The algorithm alternates shape and topology optimization steps. The underlying elliptic problem is solved using the finite element method on a triangular mesh laying on the torus.

Numerical experiences show that, for best behaviour of the algorithm, the shape optimization step should be repeated until some stability occurs and only then a topology optimization step should be performed. Otherwise, the topology

optimization procedure may produce a new hole near the boundary of a previous hole, thus causing the two holes to merge. This means a mere change in the geometry and no real change of the topology. For instance, in the second example in subsection 6.4 (see Figure 25) some topology optimization steps were applied, but resulted in a new hole joint to the extremity of the previous hole, which simply accelerated the elongation process of the existing hole.

There are examples where the topology variation is not necessary, in the sense that the topological derivative is positive in the entire cellular domain, that is no hole is nucleated. This happens when the design is quite stabilised by shape optimization (see examples in subsection 6.5).

For the minimization of the Poisson coefficient with the goal of obtaining auxetic materials, the topology variation by nucleation of holes proved inadequate. The existing holes develop sharp extremities of thickness about ℓ , the characteristic segment length of the mesh. A nucleation of a new hole usually happens on the boundary of an existing hole in a sharp region. As each new hole is supported on the triangles around a vertex, it has a diameter of about 2ℓ which is thicker than the extremities of existing holes. This destabilizes the optimization process and does not change the topology of the design. The only variation of topology happens when two holes merge.

A challenge for the authors is to implement the same algorithm and the meshing/remeshing processes for three dimensional problems. Although theoretically the generalization is straightforward, the practical side is quite laborious. A translation of the code to an object oriented language, probably C++, will be a first step for upgrading.

Acknowledgements This work was partially supported by Fundação para a Ciência e a Tecnologia, Financiamento Base 2008 - ISFL/1/209 and by the project "Análise Assintótica aplicada à Mecânica dos Meios Contínuos", PPCDT/MAT/60587/2004.

References

1. G. Allaire, Homogenization and two-scale convergence, *SIAM J. Math. Anal.*, 23, n. 6 p. 1482-1518 (1992)
2. G. Allaire, Shape Optimization by the Homogenization Method, *Applied Mathematical Sciences* 146, Springer (2002)
3. G. Allaire, F. Jouve, A.-M. Toader, Structural optimization using sensitivity analysis and a level set method, *Journal of Computational Physics*, 194, p. 363-393 (2004)
4. G. Allaire, R. Kohn, Optimal design for minimum weight and compliance in plane stress using extremal microstructures, *European Journal of Mechanics A Solids*, 12 (6), p. 839-878 (1993)
5. C. Barbarosie, Optimização de forma aplicada a materiais compósitos, in: J. M. Goicolea, C. Mota Soares, M. Pastor, G. Bugeda (editors), *Métodos Numéricos en Ingeniería V*, SEMNI, Sociedad Española de Métodos Numéricos en Ingeniería, p. 369 (2002)
6. C. Barbarosie, Shape optimization of periodic structures, *Computational Mechanics*, 30, p. 235-246 (2003)
7. C. Barbarosie, A.-M. Toader, Shape and Topology Optimization for periodic problems, Part I, The shape and the topological derivative, submitted, see also Preprint CMAF Pre-2008-016 <http://cmaf.ptmat.fc.ul.pt/preprints/preprints.html>
8. H. Eschenauer, V. Kobelev, A. Schumacher, Bubble method for topology and shape optimization of structures, *Structural Optimization*, 8, p. 42-51 (1994)
9. S. Garreau, P. Guillaume, M. Masmoudi, The topological asymptotic for PDE systems: the elasticity case, *SIAM Journal on Control and Optimization*, 39, p. 1756-1778 (2001)
10. F. Léné, G. Duvaut, Isotropy properties of homogenized media, *Comptes Rendus de l'Académie de Science Série II*, 293 (7), p. 477-480 (1981)
11. F. Murat, S. Simon, Etudes de problèmes d'optimal design, *Lecture Notes in Computer Science* 41, p. 54-62, Springer-Verlag, Berlin (1976)
12. J. Sokołowski, A. Żochowski, Topological derivatives of shape functionals for elasticity systems, *Mech. Structures Mach.*, 29, p. 331-349 (2001)
13. J. Sokołowski, J.P. Zolezio, Introduction to shape optimization: shape sensitivity analysis, *Springer Series in Computational Mathematics*, vol. 10, Springer, Berlin (1992)
14. A.-M. Toader, Optimization of Periodic Microstructures using Shape and Topology Derivatives, communication at WCCM8, EC-COMAS 2008, Venice, July 2008
15. H. Beirão da Veiga, On non-Newtonian p -fluids. The pseudo-plastic case, *J. Math. Anal. Appl.*, 344, p. 175-185 (2008)
16. S. Vigdergauz, Two-dimensional grained composites of minimum stress concentration, *International journal of solids and structures*, 34 (6), p. 661-672 (1997)